Engineering Fracture Mechanics 104 (2013) 140–161

Contents lists available at SciVerse ScienceDirect

Engineering Fracture Mechanics

journal homepage: www.elsevier.com/locate/engfracmech

Crack initiation and fracture toughness of random Voronoi honeycombs

I. Christodoulou, P.J. Tan *

Department of Mechanical Engineering, University College London, Torrington Place, London WC1E 7JE, UK

ARTICLE INFO

Article history:
Received 12 April 2012
Received in revised form 20 March 2013
Accepted 20 March 2013
Available online 2 April 2013

Keywords:
Fracture toughness
Voronoi
T-stress
Finite elements
Cellular solids
Mode-mixity

ABSTRACT

The competing effects of cell-regularity and relative density upon the toughness of Voronoi honeycombs are investigated for different loading modes using finite elements. Mode I toughness is shown to be the more sensitive to microstructural variations than mode II although both retain a strong quadratic dependence upon relative density. Crack initiation is shown to occur at up to six cells from the crack-tip in regions of high localised strain and/or high strain gradient. The inclusion of *T*-stress dramatically changes the location of ligament fracture and the normalised effective toughness of a lattice. Ligament fracture is predominantly due to bending.

1. Introduction

The increased fracture risk for patients with osteoporosis is attributed to a reduction in the mass of bone, or relative density $\overline{\rho}(\equiv \rho^*/\rho_s$ where ρ^* and ρ_s are the densities of the bone and cell wall material, respectively) [1–3]. This can be predicted by measuring the amount of bone loss in a non-invasive, dual energy X-ray absorptiometry (DEXA) scan. It is also widely suspected that variations in cell architecture, too, have an effect upon the fracture toughness of trabecular bones [3,4]. Recent studies on the defect tolerance of periodic two-dimensional (2D) and three-dimensional (3D) lattice materials have revealed that their fracture toughness is sensitive to random dispersion of the wall vertices of their corresponding perfect lattice; the knockdown in toughness depends on the cell morphology [5–7]. But it remains unclear whether the same might be observed in lattices with non-periodic cells where its macroscopic response is dominated by the bending deformation at the cell scale. The aim of the present study, which is part of a wider investigation into the osteoporotic fracture risks of trabecular bones, is to clarify how the competing influences of relative density and architectural variations affect the fracture toughness of cellular solids with a non-periodic cell morphology; an understanding of this has relevance to biomedical applications [1,3,4].

It is well-known that the mode I toughness (K_{IC}) of a perfect, *elastic-brittle*, hexagonal honeycomb scales with relative density $\overline{\rho}$, the characteristic length of the cell l and the fracture strength of the cell wall material σ_f in accordance to

$$K_{IC} = D\overline{\rho}^d \sigma_f \sqrt{l}. \tag{1}$$

Eq. (1) assumes that crack advancement occurs when the cell wall immediately ahead of the crack-tip fractures and is valid for any crack length greater than seven-cells [1,8,9]. For periodic 2D lattices, it was shown in [5,6] that the severity of imper-

* Corresponding author. Tel.: +44 (0)20 7679 3754; fax: +44 (0)20 7388 0180.
E-mail address: pj.tan@ucl.ac.uk (P.J. Tan).

0013-7944/$ - see front matter © 2013 Elsevier Ltd. All rights reserved.
http://dx.doi.org/10.1016/j.engfracmech.2013.03.017

Nomenclature

A	lattice area
B	stress biaxiality ratio
E_s, E^*	elastic modulus of cell wall material and honeycomb
G_s, G^*	shear modulus of cell wall material and honeycomb
$\mathcal{G}$	energy release rate
I	isotropy parameter
K_I, K_{II}	mode I and II stress intensity factor (SIF)
K_{IC}, K_{IIC}	mode I and II fracture toughness
K_{eff}, $K_{eff,C}$	effective and critical effective stress intensity factor
l, $\bar{l}$	characteristic and average cell wall length
M	mode-mixity parameter
m	number of cells in a honeycomb
r	distance from crack tip
T	T-stress
t	cell wall thickness
U_b, U_a, U_s	strain energy due to bending, axial stretch and shear
u_1, u_2	displacement in the x_1 and x_2 directions
x_1, x_2	cartesian coordinates with origin centred at crack tip
α	crack length
ϵ_{ij}	strain
η	ratio of bending to total strain energy
θ	polar angle
Λ	cell-regularity parameter
ν^*	Poisson's ratio of honeycomb
$\overline{\rho}$	relative density
ρ_s, ρ^*	density of cell wall and lattice material
σ_f	tensile fracture strength of cell wall
σ_{ij}	stress
σ_{max}	maximum tensile stress in an element

Sub/superscripts

s	material properties of cell wall
$*$	elastic in-plane properties of honeycomb
ps	plane strain properties

fections and loading mode influence the pre-exponent D whilst the exponent d depends on the dominant mode of deformation at the cell scale; Fleck and Qiu [5] found that d=1 and d=0.5 for perfect triangular and Kagome lattices, respectively. The same form of scaling law also applies to periodic 3D lattices [7]. However, the toughness of these perfect lattices are highly sensitive to imperfections in their microstructure; for example, misalignment of wall vertices in a regular hexagonal honeycomb can lead to a knockdown in its mode I toughness K_{IC} by up to 40% [6]. By contrast, cellular solids with a non-periodic cell morphology, such as trabecular bones or stochastic foams, deform primarily by cell wall bending. Consequently, their mode I toughness K_{IC} is anticipated to scale with $\overline{\rho}^2$ although it is unclear to what extent increasing cell irregularity affects the pre-exponent D under different loading modes. Also, the effects of cell regularity upon the location of fracture initiation and the influence of T-stress upon their effective toughness have not previously been studied and are not well understood; these will be investigated here.

The focus of this paper will be on random 2D lattices generated by a Voronoi construction. Whilst it is recognised that the cell walls in trabecular bones follow the trajectories of principal stresses and it is the mechanical efficiency that shapes its structure [1], a Voronoi lattice has alluring micro-architectural features reminiscent of those seen in real bones. It is easily generated and deforms primarily by cell wall bending when loaded; this is why a Voronoi construct is widely used as a 2D representation of the non-periodic cell microarchitecture of natural cellular solids [1,10–13]. Moreover, the regularity of its cells can be controlled through a non-dimensional parameter, to be introduced in the following section, which would allow the competing roles of relative density loss and microstructural deterioration to be investigated. Therefore, 2D Voronoi lattices will be studied here to gain insights into the fracture response of natural cellular solids, such as trabecular bones.

This paper considers the asymptotic problem of an *elastic-brittle* Voronoi lattice (of relative density $0.001 \leqslant \overline{\rho} \leqslant 0.3$) containing a long, plane-strain crack subject to a displacement field, associated with the macroscopic K-field of linear elastic fracture mechanics (LEFM), which is applied at the remote boundary of the lattice. The regularity of the cells within the lattice is controlled by a non-dimensional scalar measure Λ which places a constraint on the minimum cell size and the spread of the cell size distribution. This approach allows the response of lattices with different cell regularity, but of identical

relative density, to be compared. The aim is to quantify the sensitivity of the macroscopic lattice toughness in different loading modes and the location of fracture initiation to the different competing influences of cell-regularity Λ and relative density $\overline{\rho}$. The effects of T-stress (the non-singular stress parallel to the crack plane) to the above are also investigated.

This paper is structured as follows. Section 2 introduces a non-dimensional scalar measure Λ to generate δ- and Γ-Voronoi honeycombs of varying cell-regularity. Their in-plane elastic properties are first obtained and the assumption of isotropy assessed. Macroscopic fracture toughness of the 2D lattices are presented in Section 3 and the effects of mode mixity upon the location of fracture initiation is explored for different Λ. The effects due to T-stress inclusion are explored in Section 4. Section 5 presents fracture map that shows the location of fracture initiation for different realisations of lattices with the same regularity. Finally, in Section 6, continuous strain maps are generated to elucidate the deformations in regular and random lattices for different combinations of mode mixity and T-stress.

2. Voronoi lattices and their in-plane elastic properties

2.1. Definition of cell regularity

Denote the Euclidean distance between any two points p and q in 2D space by $dist(p,q) \equiv \sqrt{\left(x_1^p - x_1^q\right)^2 + \left(x_2^p - x_2^q\right)^2}$ and let $P := \{p_1, p_2, \ldots, p_m\}$ be a set of m distinct random points on a plane (the domain), referred to hereinafter as nuclei, where $dist(p_i,p_j) \neq 0 \forall i \neq j$. If the plane is subdivided into m number of cells, one for each nuclei in the set P, according to the assignment rule where a point q in the cell corresponding to a nuclei p_i if and only if $dist(q,p_i) < dist(q,p_j)$ for each $p_j \in P$ with $j \neq i$, the resulting 2D lattice is commonly known as a Voronoi honeycomb [1,14]. This assignment model places no constraint on the final cell shape and size, or its distribution, and assumes that all cells nucleate at the same time and grow at the same linear growth rate. If, however, a constraint is imposed on the minimum distance d_{min} between any two nuclei in P, i.e. $dist(p_i,p_j) \geqslant d_{min} \forall i \neq j$, this would generate a Voronoi honeycomb with greater cell regularity [1].

A regular hexagonal lattice is a special case of a Voronoi honeycomb if each nuclei in the set P is always surrounded by six immediate neighbours, all separated by an equal distance of

$$d_0 = \sqrt{\frac{2A}{m\sqrt{3}}} \tag{2}$$

and at equal angles of 60° from one another. In other words, the m nuclei are arranged in a regular hexagonal configuration separated by equidistant d_0 within the planar area A. Following Zhu et al. [15], a non-dimensional constant

$$\Lambda \equiv \frac{d_{min}}{d_0} \tag{3}$$

defined on the interval $(0,1]$, hereinafter referred to as a cell-regularity parameter, is introduced as a scalar measure to describe, an otherwise, randomly generated 2D Voronoi lattice. The two limiting cases of $\Lambda \to 0^+$ and $\Lambda = 1$ correspond to when there is no minimum imposed distance between any two nuclei in the set P, resulting in a completely random Γ-Voronoi honeycomb, and one where there is a maximum imposed distance, resulting in a regular hexagonal honeycomb, respectively.

Fig. 1 shows Voronoi lattices for a range of Λ, generated using the assignment model described above. It is also worth noting that all the cells in a 2D Voronoi lattice, regardless of regularity, are always convex which is unlike those generated by random cell node perturbation of a regular lattice, such as that used by Romijn and Fleck [6]. The introduction of Λ provides a useful means by which to control the cell-regularity in a random 2D lattice, allowing a systematic investigation into the effects of cell-regularity on the macroscopic toughness of the lattices. It must, however, be acknowledged that the cell shape in trabecular bones, which is the motivation behind this study, is controlled by other criteria different to the one here [1]. Notwithstanding, the study of 2D Voronoi lattices is a useful first step to elucidate the effects of cell-regularity upon the toughness of more complicated 3D lattices with convex cells.

2.2. Relative density

The relative density of the Voronoi lattices, assuming uniform cell wall thickness t, is calculated using:

$$\overline{\rho} = \frac{t\sum_{i=1}^{N} l_i}{A} \tag{4}$$

where l_i is the length of the i^{th} cell wall in a lattice with N number of cell walls. The wall thickness in Eq. (4) is adjusted separately for each lattice to achieve the desired $\overline{\rho}$ value. This is necessary when studying the influence of Λ since comparisons must be made between lattices of the same relative density. Alternatively, it is also possible to achieve the desired $\overline{\rho}$ by adjusting the length l_i of each cell wall proportionally since $\overline{\rho} \propto t/\hat{l}$. It will be shown in Section 3.2 that either approach makes no difference to the pre-exponent D of both regular and irregular lattices, since the analysis will be carried out in a deterministic framework similar to that employed in [5,6]. For convenience, the regular lattice is assumed to have unit cell wall length in this study. Cell randomness has the effect of increasing the average cell wall length in a lattice. Table 1 shows

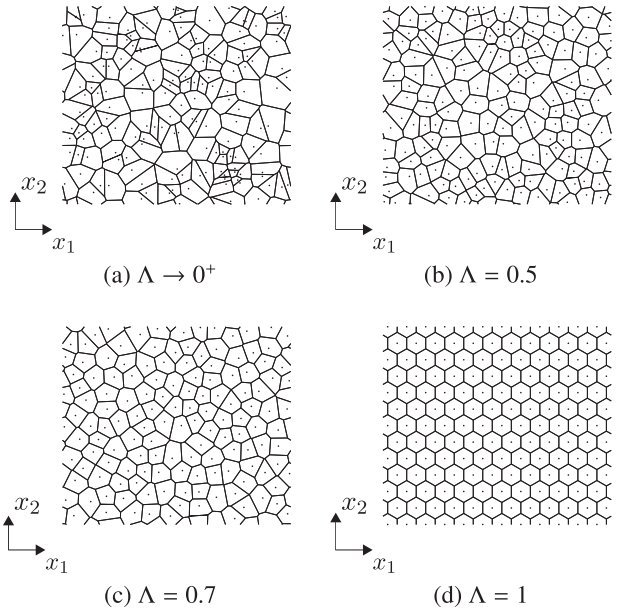

Fig. 1. Randomly generated Voronoi honeycombs with different cell-regularity. Each lattice comprises of approximately 150 cells. The nucleus of each cell is indicated by a dot.

Table 1
Typical average cell wall length in random lattices of various cell-regularity.

Λ	$\to 0^+$	0.25	0.5	0.6	0.7	0.8	1
$\hat{l}$	1.0775	1.0754	1.0636	1.0575	1.0484	1.0374	1

how the average wall length $\hat{l}$ increases with decreasing cell regularity. The difference in $\hat{l}$ is less than 8% between the two limiting cases of $\Lambda \to 0^+$ and $\Lambda = 1$.

2.3. In-plane elastic properties

2.3.1. Regular lattice ($\Lambda = 1$)

The in-plane elastic properties of a regular lattice where $\Lambda = 1$ (Fig. 1d) are given by [1]:

$$E^* = \frac{3}{2}\overline{\rho}^3 E_s, \quad G^* = \frac{3}{8}\overline{\rho}^3 E_s, \quad v^* = 1 \tag{5}$$

where the superscript $*$ and subscript s denotes the honeycomb and cell wall material properties, respectively. A regular lattice is isotropic with identical stiffness ($E_1^* = E_2^*$) and Poisson's ratio ($v_{12}^* = v_{21}^*$) in the x_1 or x_2 directions. Just like an isotropic fully dense material, their Poisson's ratio and elastic moduli are also related through $G^* = E^*/2(1 + v^*)$. Since the scaling laws in Eq. (5) were derived using the simple beam bending theory, they are valid only for relatively low values of $\overline{\rho}$. At higher values, say $\overline{\rho} \geqslant 0.15$, the aspect ratio of the cell walls no longer justifies omission of the shear and axial wall stresses; in such cases, Eq. (5) should be replaced with the theoretical estimates presented in Silva et al. [10]. The typical error caused by neglecting shear and axial wall stresses is approximately 10% for a regular lattice with $\overline{\rho} \approx 0.15$; this error increases with $\overline{\rho}$.

2.3.2. Irregular lattices ($\Lambda \neq 1$)

For irregular lattices where $\Lambda \neq 1$ (Fig. 1a–c), Eq. (5) is no longer applicable since $\overline{\rho}$ does not scale with the geometry of the random cell aggregate in the manner proposed by Gibson and Ashby [1]. Notwithstanding, it would be obvious later that their in-plane elastic properties remain strongly dependent upon $\overline{\rho}$. Finite element calculations were first performed to establish how the elastic properties of the lattices vary under the competing influences of Λ and $\overline{\rho}$. The results will be used as inputs to calculate the plane-strain fracture toughness of the lattices under combined mode I and mode II loadings, to be discussed in Section 3.

2.3.3. Finite element model

To investigate the effects of the random cell topology, a sufficiently large sample of Voronoi tessellations were created for each cell-regularity to be investigated – see Section 2.3.4. A square finite element (FE) mesh of each tessellation is generated using the software ABAQUS/standard®. Periodic boundary conditions (BCs) were imposed on the lattice boundaries according to

$$u_i^p - u_i^q = \epsilon_{ij}\left(x_j^q - x_j^p\right), \quad \omega^p - \omega^q = 0 \tag{6}$$

where $i, j = 1, 2$ denote degrees of freedom and p, q refer to the nodes on opposing sides of the lattice. This is necessary since the use of mixed BCs is known to under-estimate the elastic moduli of the lattices [15,16]. Convergence studies were performed where it was found that the use of four Timoshenko beam elements (B21) per cell wall in a lattice comprising of 50×50 cells gives sufficiently accurate results. All numerical simulations were performed in the context of small strains and rotations.

2.3.4. Numerical predictions

Elastic properties for the lattices were obtained under plane-stress loading conditions where $\sigma_{13} = \sigma_{23} = \sigma_{33} = 0$. The elastic moduli were normalised with $\overline{\rho}^3 E_s$ to give $\overline{E}^*$ and $\overline{G}^*$. Table 2 shows the average elastic properties and the percentage variation, from their respective mean values, for the different loading directions. The data shown were obtained from a sample of twenty tessellations with constant cell-regularity $\Lambda = 0.5$ and relative density $\overline{\rho} = 0.1$. Numerical checks have been performed to verify that a sample size of, at least, twenty tessellations is needed at each cell-regularity to give representative results. The differences between the average properties in the x_1 and the x_2 direction are generally insignificant. Likewise, the percentage variations of the average elastic moduli and Poisson's ratio are, similarly, insignificant; <2% and <0.5%, respectively, for all combinations of $\overline{\rho} - \Lambda$ considered in this study. These results are not surprising since the cells in a Voronoi lattice have no preferred orientation. Therefore, the $\overline{E}_1^*$ and $\overline{E}_2^*$ values of each lattice are combined into a single data set of 40 samples with only its mean value plotted in Fig. 2a: the same applies to $v_{12}^* - v_{21}^*$ which are plotted in Fig. 2c.

Fig. 2a and b shows the variation of the elastic moduli with $\overline{\rho}$ and Λ. The theoretical estimates by Silva et al. [10] are nearly identical to the present FE results for regular lattices. At the lower values of $\overline{\rho}$, cell-irregularities lead to an increase in $\overline{E}^*$ and $\overline{G}^*$ by up to 20% as $\Lambda \to 0^+$. This trend is reversed for relative densities $\overline{\rho} > 0.2$. The variations of each data point plotted in Fig. 2a and b are less than one standard deviation and this also agrees well with the results of Silva et al. [10] and Zhu et al. [15].

The Poisson's ratio v^* of a lattice decreases with increasing $\overline{\rho}$ as shown in Fig. 2c; this trend is similar to the theoretical estimate in [10] for regular lattices. Cell-irregularity does not appear to have a significant effect on v^*, leading only to a slightly reduced v^* as $\Lambda \to 0^+$; this reduction becomes more pronounced at higher values of $\overline{\rho}$. Note that a similar trend is also reported by Zhu et al. [15]. Fig. 2d shows the variation of $I = 2G^*(1 + v^*)/E^*$, an isotropy parameter, with $\overline{\rho}$. As expected, I is always unity for a regular lattice regardless of its relative density. For irregular lattices, I is only slightly raised (<5%). Therefore, the assumption of an isotropic 2D lattice for every cell-regularity parameter Λ is, to a first approximation, valid.

3. Fracture toughness

3.1. Methodology and finite element model

The in-plane stress field of a linear elastic cracked body is given by [17]:

$$\sigma_{ij} = C_1 g_{ij}^{(1)}(\theta)\frac{1}{\sqrt{r}} + C_2 g_{ij}^{(2)}(\theta) + C_3 g_{ij}^{(3)}(\theta) r^{1/2} + \sum_{n=4}^{\infty} C_n g_{ij}^{(n)}(\theta) r^{(n-2)/2} \tag{7}$$

where σ_{ij} is the stress tensor, $r - \theta$ are polar coordinates centred at the crack tip, $g_{ij}^{(n)}(\theta)$ are dimensionless functions of θ and C_n is its corresponding stress amplitude. In the immediate crack-tip region, the singular stress field given by the leading term of Eq. (7) can be decomposed additively into contributions from remote tensile (Mode I) and in-plane shear (Mode II) loadings as [18]

$$\sigma_{ij} = \frac{K_{\mathrm{I}}}{\sqrt{2\pi r}}\hat{\sigma}_{ij}^{\mathrm{I}} + \frac{K_{\mathrm{II}}}{\sqrt{2\pi r}}\hat{\sigma}_{ij}^{\mathrm{II}} \tag{8}$$

Table 2
The average elastic moduli and Poisson's ratio obtained from a sample of twenty Voronoi tessellations. All lattices have identical cell-regularity $\Lambda = 0.5$ and a relative density of $\overline{\rho} = 0.1$.

	$\overline{E}_1^*$	$\overline{E}_2^*$	$\overline{G}^*$	v_{12}^*	v_{21}^*
Mean	1.5866	1.5910	0.4152	0.9689	0.9668
% Deviation	1.5674	1.5658	1.3934	0.2081	0.4376

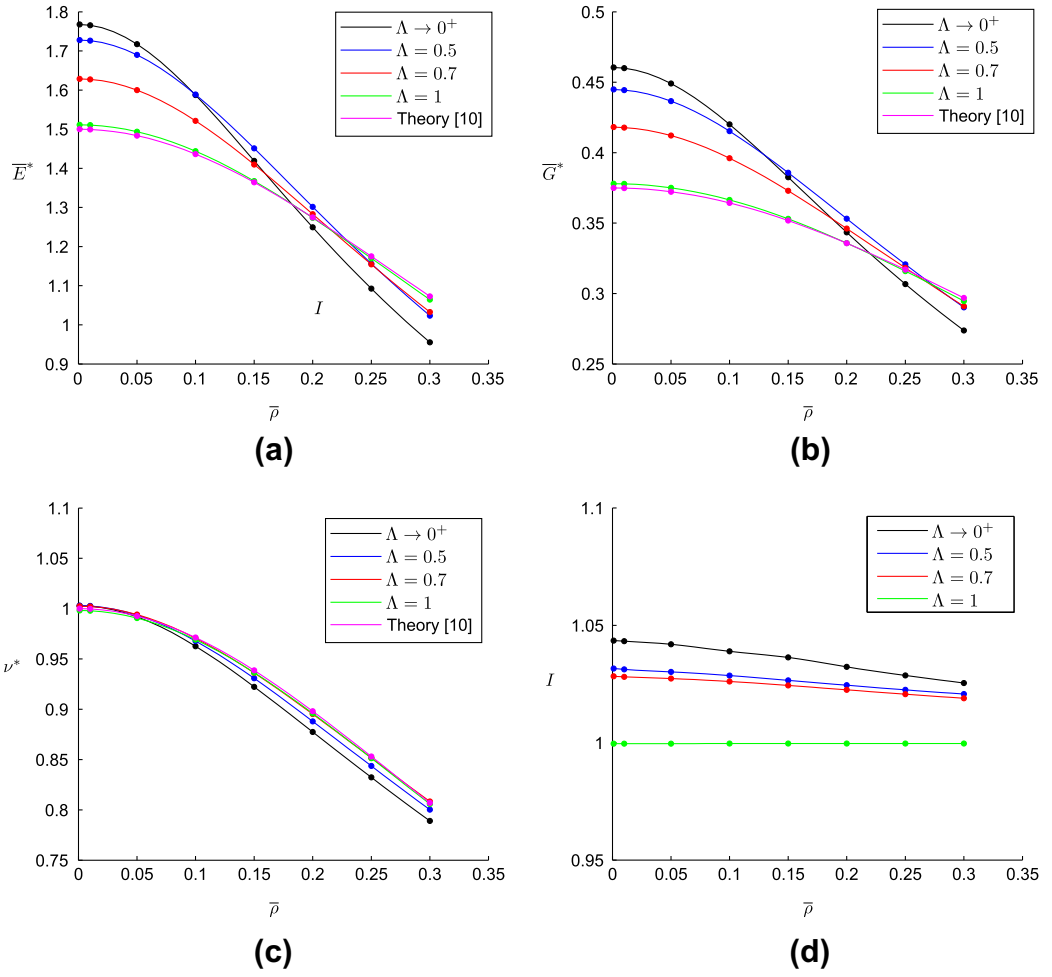

Fig. 2. In-plane elastic properties and isotropy parameter as a function of relative density $\overline{\rho}$ for different cell-regularity parameter Λ. Theoretical estimates of $\overline{E}^*, \overline{G}^*$ and ν^* for a regular lattice by Silva et al. [10] are included for comparison.

where K_{I} and K_{II} are the mode I and mode II stress intensity factors (SIFs), respectively. The displacement components (u_1, u_2) associated with the asymptotic crack-tip field (in Eq. (8)) for a plane-strain crack in an elastic solid are given by [18]:

$$u_i = \frac{1}{2G^*_{\mathrm{ps}}}\sqrt{\frac{r}{2\pi}}[K_{\mathrm{I}}\hat{u}_i(\theta, \nu^*_{\mathrm{ps}})^{\mathrm{I}} + K_{\mathrm{II}}\hat{u}_i(\theta, \nu^*_{\mathrm{ps}})^{\mathrm{II}}]; \quad i = 1, 2 \tag{9}$$

where $\hat{u}_i(\theta, \nu^*_{\mathrm{ps}})^{\mathrm{I}}$ and $\hat{u}_i(\theta, \nu^*_{\mathrm{ps}})^{\mathrm{II}}$ are functions of the angle θ and the plane-strain Poisson's ratio ν^*_{ps} of the lattices. For mixed-mode loading, the relative composition of K_{I} and K_{II} is controlled by means of an elastic mode-mixity parameter M defined by [19]:

$$M = \frac{2}{\pi}\tan^{-1}\left(\frac{K_{\mathrm{II}}}{K_{\mathrm{I}}}\right); \quad 0 \leqslant M < 1 \tag{10}$$

where the limiting values of $M = 0$ and $M \to 1^-$ corresponds to the mode I and mode II fracture toughness, respectively.

Fig. 3 shows a schematic of a typical Voronoi lattice ($\Lambda = 1$) with $n \times n$ cells that were implemented in ABAQUS/standard®. A long plane-strain crack of $n/2$ cell-length, with its tip located at the nucleation point of the crack-tip cell, is assumed to align with the negative x_1 axis. The displacements associated with the asymptotic crack-tip field given by Eq. (9) were applied to the boundary nodes of the FE mesh. This is also the approach employed in [5,6]. By imposing the K-displacement field to the lattice boundary, it is tacitly assumed that the lattice is isotropic and homogeneous. Since the elastic properties in Fig. 2 were obtained under plane-stress conditions, they need to be modified for use in Eq. (9). Supposing the elastic modulus of the lattices in the prismatic x_3 direction is $E_{33} = \overline{\rho}E_s$ and its Poisson's ratio is $\nu_{31} = \nu_{32} = \nu_s$, then under plane-strain conditions, with $\epsilon_3 = 0$ and $\sigma_3 = \nu_{31}\sigma_1 + \nu_{32}\sigma_2$, the modified elastic moduli and Poisson's ratio become as follows:

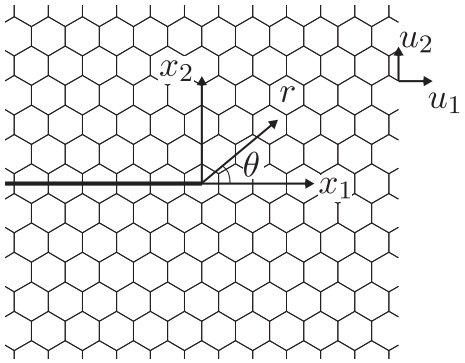

Fig. 3. Schematic of the FE model with a long plane-strain crack aligned along the negative x_1 axis. The Cartesian coordinates $x_1 - x_2$ and polar coordinates $r - \theta$ are centred at the crack-tip as shown.

$$E^*_{ps} = \frac{2E^*}{2 - 3\overline{\rho}^2 v_s^2}, \quad v^*_{ps} = \frac{2 + 3\overline{\rho}^2 v_s^2}{2 - 3\overline{\rho}^2 v_s^2}, \quad G^*_{ps} = \frac{E^*_{ps}}{2\left(1 + v^*_{ps}\right)} \tag{11}$$

The same finite element mesh, described earlier in Section 2.3.3, is used here to evaluate the lattice toughness. A crack is generated along the negative x_1-axis by splitting the beams at $x_2 = 0$ so that no connection exists across the traction-free crack plane. Numerical checks were carried out which show that it suffices to model each cell wall with four Timoshenko beams elements (B21) without any loss of accuracy.

A deterministic approach, similar to that employed in [5–7], is adopted here to evaluate the macroscopic fracture toughness of the lattices. The cell walls in the lattice are assumed to be elastic-brittle with no dependence on scale, i.e. failure always occurs at the same maximum stress regardless of the dimensions of the cell wall. For such an idealised material, failure occurs when the local stress at the outermost fibre of any beam element in the lattice reaches the cell wall fracture strength of σ_f. Unlike in Huang and Gibson [9], the present study ignores the effects of flaws on the fracture strength of the brittle cell wall. Using this simple deterministic framework, the macroscopic fracture toughness of the Voronoi lattices was found to be sensitive to the overall specimen size. Fig. 4 shows how the mode I fracture toughness of a regular lattice ($\Lambda = 1$) varies with the overall specimen size (of $n \times n$ cells). The same also applies to irregular lattices. As a compromise between computational time and numerical accuracy, all simulations were performed with lattices of 200×200 cells. Similar to Section 2.3.4, numerical checks were carried out which also showed that, at least, twenty tessellations are needed at each value of Λ in order to obtain representative values for the toughness. Hereinafter, unless stated otherwise, the lattice toughness at each Λ is an average of twenty tessellations.

3.2. Mode I and mode II fracture toughness

In this section, the sensitivity of the lattice toughness to cell-regularity and relative density are evaluated for pure mode I and II loadings. Fig. 5 shows the deformed FE mesh for Voronoi lattices, of a constant relative density $\overline{\rho} = 0.1$, with different

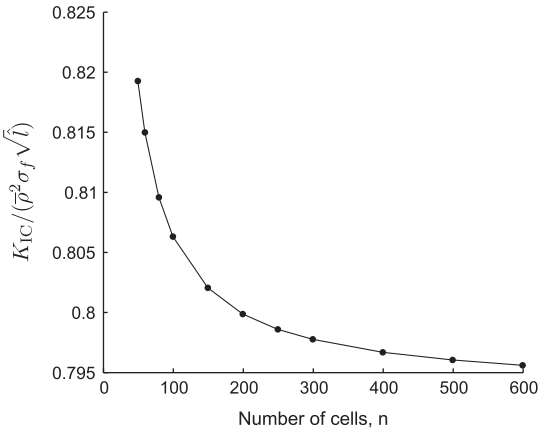

Fig. 4. Typical variation of the mode I fracture toughness of a regular lattice with overall lattice size of $n \times n$ cells.

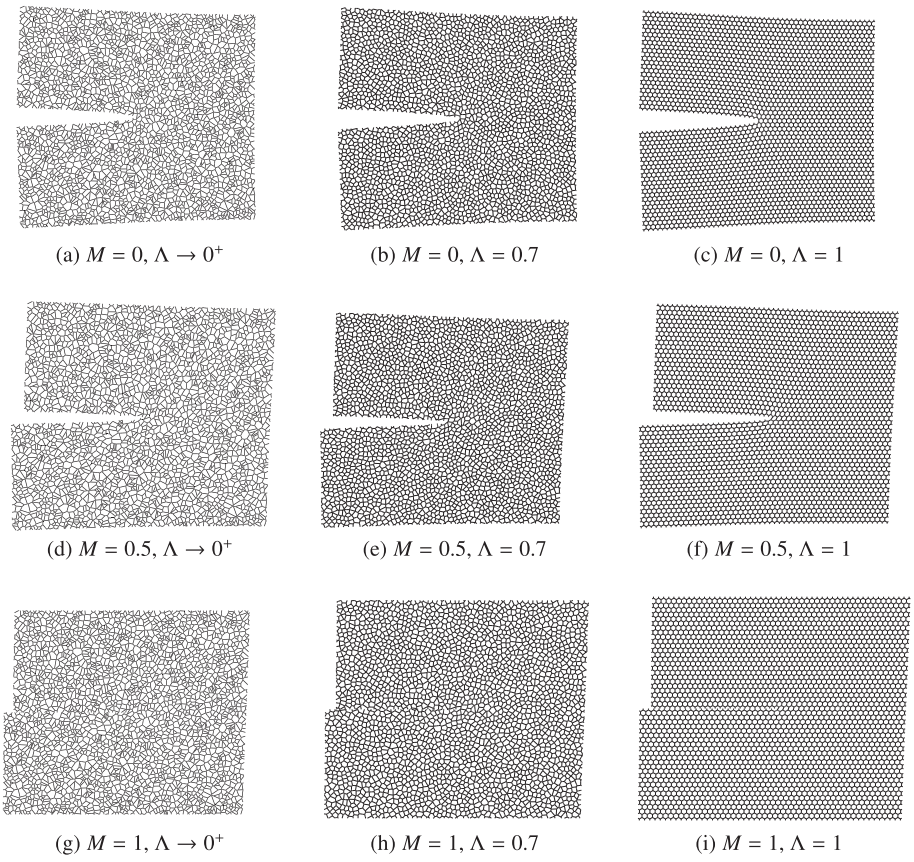

Fig. 5. Typical lattice deformation under mode I, mixed-mode and mode II loadings. The lattice shown have cell-regularity of $\Lambda \to 0^+$, $\Lambda = 0.7$ and $\Lambda = 1$. All lattices have the same relative density of $\overline{\rho} = 0.1$.

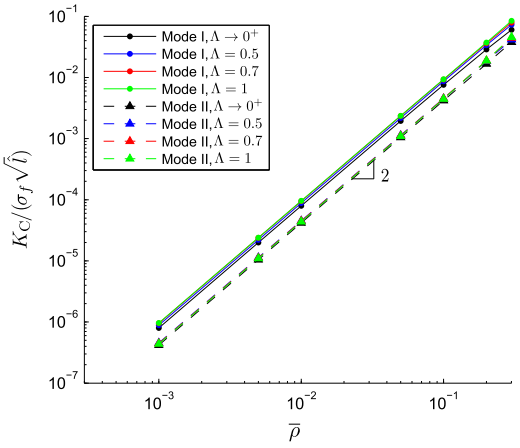

Fig. 6. Fracture toughness of lattices with different cell-regularity against relative density.

cell-regularity ($\Lambda \to 0^+, 0.7, 1$) subjected to pure mode I/II and mixed mode ($M = 0.5$) loadings. Only 50×50 cells are shown in each case; these were cropped from larger lattices of 200×200 cells.

The average fracture toughness of the lattices were fitted to the scaling law [1,5]

$$\frac{K_C}{\sigma_f\sqrt{l}} = D\overline{\rho}^d \tag{12}$$

and plotted on a log–log scale in Fig. 6. Note that Eq. (12) uses the average cell wall length $\hat{l}$ from Table 1. Recall that for the irregular lattices, their toughness is an average of twenty tessellations but their respective error bars are not shown for the sake of clarity. Fig. 6 shows that the predicted lattice toughness fits well the scaling law of Eq. (12) with the fitted coefficients tabulated in Table 3.

Regardless of cell-regularity or the loading mode, the fracture toughness K_C has a near quadratic dependence upon $\overline{\rho}$. This is to be expected since a Voronoi lattice, whether regular or irregular, has an average nodal connectivity of 3 and, therefore, they deform primarily by cell wall bending, with only a negligible contribution from axial stretch of between 3% and 10% at the fracture site, see Section 6.2. The effects of cell-regularity upon the lattice toughness is determined by the parameter D which is given in Table 3. It shows that the average mode I toughness is more sensitive to cell regularity than its corresponding mode II counterpart.

Fig. 7 plots $K_C/(\sigma_f\overline{\rho}^2)$ against $\hat{l}$ for lattices with the same relative density $\overline{\rho} = 0.1$. The square root dependence of $K_C/(\sigma_f\overline{\rho}^2)$ on the average cell wall length $\hat{l}$ (see Eq. (12)) is the same for both regular and irregular lattices with identical $\overline{\rho}$ but different $\hat{l}$. Therefore, adjusting either their wall thickness uniformly (as is used in this study) or their average wall length proportionally to obtain the required $\overline{\rho}$ has no effect upon the pre-exponent D in Eq. (12) so long as the analysis is carried out in a deterministic framework similar to that in [5,6].

Fig. 8 shows the variation of the average non-dimensional toughness $K_C/(\sigma_f\overline{\rho}^2\sqrt{\hat{l}})$ with cell-regularity for pure mode I and mode II loadings. Again, each data point is the average of twenty tessellations and the error bar corresponds to their standard deviation. The effect of relative density is eliminated by non-dimensionalisation so the two plots for $\overline{\rho} = 0.05$ and 0.1 nearly collapse on each other. One observes an almost linear reduction in the average mode I toughness with decreasing cell regularity, by up to 25% between $\Lambda = 1$ and $\Lambda \to 0^+$. Note that a 15% reduction in relative density would be needed to achieve a corresponding reduction in the toughness of a regular hexagonal honeycomb ($\Lambda = 1$). This suggests that cell regularity has a significant effect upon the mode I toughness of the lattices. No inference could be made for mode II loading since the fluctuations in toughness are nearly the same at all Λ. By contrast, as the cells become more irregular, the average in-plane elastic moduli of the lattices increases by up to 20% between $\Lambda = 1$ and $\Lambda \to 0^+$; this increase depends on $\overline{\rho}$ (see Fig. 2). For the range of $\overline{\rho}$ considered, Fig. 8 shows that Voronoi lattices, whether regular or irregular, have a greater resistance to fracture in mode I compared to mode II. Similarly, the lattice toughness also appears to be more sensitive to variations in cell-regularity for mode I than mode II loading. Since the former has a consistently higher variability than the latter, and the same twenty tessellations were used in the FE simulations for both mode I and mode II loadings at each Λ, one can conclude that the mode I toughness must be more sensitive to cell topological variations in the vicinity of the crack tip. In general, the toughness can vary by up to ±20% from the mean value between tessellations. One reason for the high variability is because cell fracture can initiate several cells away from the crack tip, depending on the local cell topology, as will be shown in Sections 5 and 6.

Romijn and Fleck [6] reported that for lattices with $\overline{\rho} = 0.01$, there is a 30% reduction in their average K_{IC} value and a 20% increase in their average K_{IIC} value if the vertices of each cell in a regular hexagonal honeycomb were allowed to vary randomly by up to a maximum distance of $l/2$, i.e. half the regular cell edge length. Note, however, that the lattice generated using the cell node perturbation technique in [6] would still give a substantively less random cell structure (measured in terms of the variation of the cell areas) than a Voronoi lattice of $\Lambda = 0.5$. Yet, the reduction in the average K_{IC} value for a Voronoi lattice is less than 10% between $\Lambda = 1$ and $\Lambda = 0.5$, while K_{IIC} remains largely unaffected. The reason for this discrepancy is unclear although one possibility is that the cells in a 2D Voronoi lattice, regardless of regularity, are always convex unlike those generated by the random cell node perturbation technique in [6] where the local Poisson's ratio may sometimes be negative.

3.3. Mixed-mode fracture toughness

In this section, the effects of relative density and cell-regularity on the lattice toughness are explored for mixed-mode loading ($M \neq 0$ or 1). The decoupling of modes in isotropic elasticity (it was shown in Section 3 that the lattices can be considered isotropic) allows the total energy release rate $\mathcal{G}$ for combined mode cracking to be written as:

$$\mathcal{G} = \frac{K_I^2}{E_{ps}^*} + \frac{K_{II}^2}{E_{ps}^*} + \frac{K_{III}^2}{2G_{ps}^*} \tag{13}$$

from which, by setting $K_{III} = 0$, an effective SIF can be defined as follows:

Table 3
Fitted coefficients using the scaling law given in Eq. (12).

	Λ	0	0.25	0.5	0.6	0.7	0.8	1
Mode I	d	1.974	1.987	1.988	1.987	1.981	1.987	1.994
	D	0.691	0.790	0.825	0.795	0.836	0.887	0.927
Mode II	d	2.001	2.010	2.004	2.015	2.010	2.013	2.019
	D	0.420	0.442	0.461	0.479	0.480	0.480	0.486

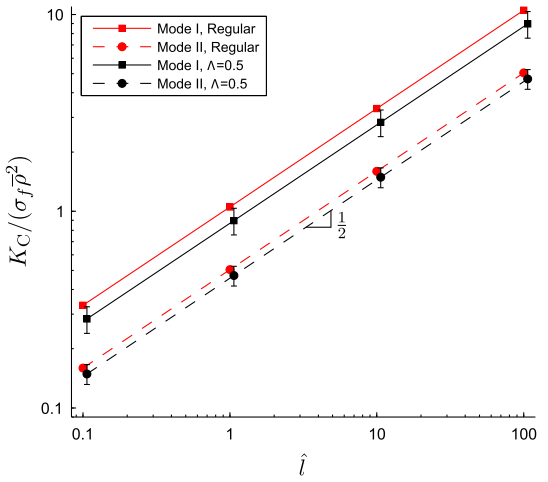

Fig. 7. Variation of normalised fracture toughness $K_C/(\sigma_f\overline{\rho}^2)$ against average cell wall length $\hat{l}$ for irregular ($\Lambda = 0.5$) and regular hexagonal ($\Lambda = 1$) lattices, subjected to mode I and mode II loadings. For the irregular lattices, each data point is the average of twenty tessellations and the error bar indicates standard deviation. Relative density is kept constant at $\overline{\rho} = 0.1$ for all cases.

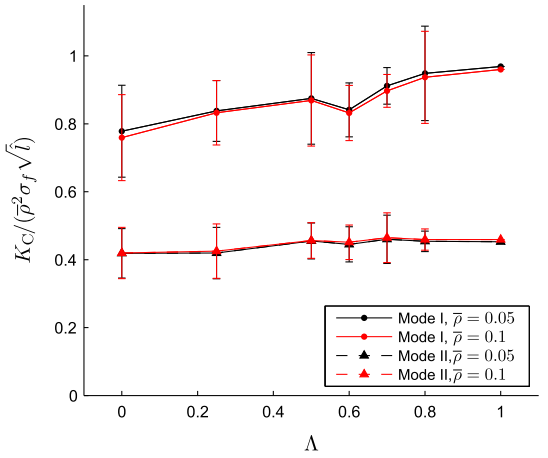

Fig. 8. Variation of non-dimensional fracture toughness $K_C/(\sigma_f\overline{\rho}^2\sqrt{\hat{l}})$ against cell-regularity for lattices with $\overline{\rho} = 0.05, 0.1$ subjected to mode I and mode II loadings. Each data is an average of twenty tessellations and the error bar indicates standard deviation.

$$K_{\text{eff}} = \sqrt{K_{\text{I}}^2 + K_{\text{II}}^2} \tag{14}$$

At each mode-mixity M, the combination of K_{I} and K_{II} needed for a single cell wall to fracture were used to calculate the critical effective SIF, $K_{\text{eff,C}}$, of the Voronoi lattice. This was repeated for a range of cell-regularity to generate the fracture loci in Fig. 9. The loci plotted are for a constant $\overline{\rho} = 0.1$ and each data point, except those at $\Lambda = 1$, is the average of 20 tessellations. It must be noted that the fracture loci are insensitive to relative density for the range of $\overline{\rho}$ investigated.

The fracture locus of a regular lattice comprises of two distinct straight segments separated by a kink at $M \approx 0.15$ – the same is reported by Fleck and Qiu [5]. This kink coincides with a shift in the cell wall fracture location as mode-mixity changes. Although a switch in fracture location, sometimes multiple switches, also occurs for the irregular lattices, the absence of kink(s) in their corresponding loci in Fig. 9 is a consequence of smoothing by averaging twenty tessellations. In general, the smoothed loci appears as a quarter ellipse that are largely similar for different values of Λ. To clarify the above, the loci of four separate tessellations at $\Lambda = 0.5$ are plotted in Fig. 10a. Without averaging, the loci remain inner convex envelopes, but unlike in Fig. 9, are a series of straight segments separated at multiple kink(s), each corresponding to a shift in the cell wall fracture location at that mode-mixity. Fig. 10b shows the lattice topology for tessellation 1 where fracture initiates at A if mode-mixity $M < 0.14$, at B if $0.14 \leqslant M \leqslant 0.6$ and at C if $M > 0.6$. Note that the number of kinks and at which mode-mixity it appears vary from one tessellation to another without a set pattern for the irregular lattices: this contrasts with a regular one.

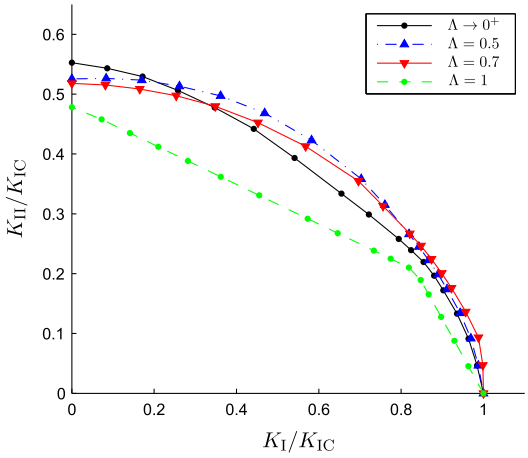

Fig. 9. The normalised fracture loci for regular and irregular Voronoi lattices. All lattices have the same relative density of $\overline{\rho} = 0.1$. Note that each data point corresponding to $\Lambda \neq 1$ is the average of twenty tessellations.

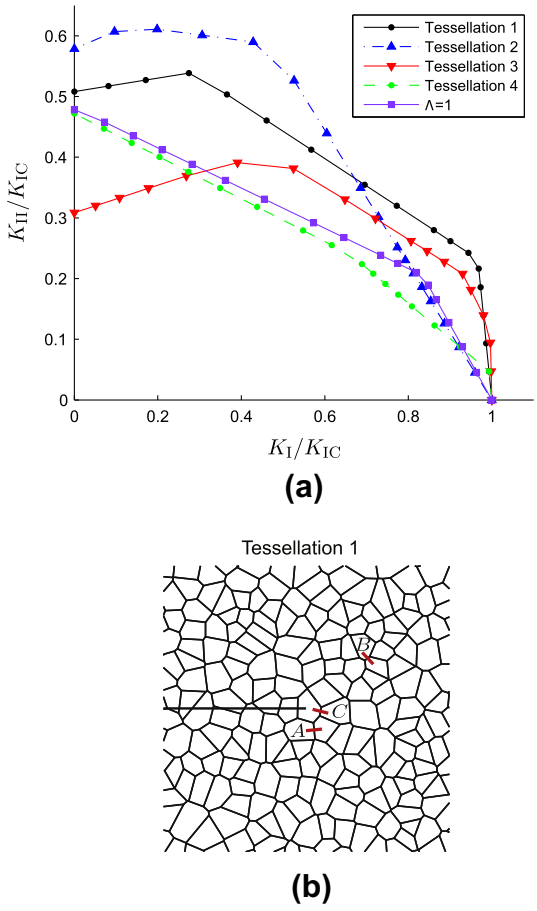

Fig. 10. (a) Normalised fracture locus of four typical Voronoi tessellations generated for Λ = 0.5. (b) The three straight segments comprising the locus of tessellation 1 in (a) correspond to the different fractured cell wall location shown as A and B.

Fig. 11 shows that, on average, the critical effective SIF ($K_{\mathrm{eff,C}}$), of both regular and irregular lattices, reduces with increasing mode-mixity M. The ratio $K_{\mathrm{eff,C}}/K_{\mathrm{IC}}$ does not vary considerably between the different irregular lattices for different mode mixity; however, they are noticeably higher than that of the regular hexagonal lattice. Note that the data in Fig. 11 are the

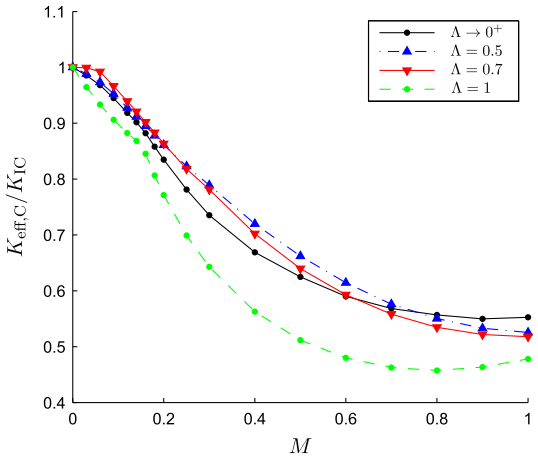

Fig. 11. The average variations of $K_{\mathrm{eff,C}}/K_{\mathrm{IC}}$ with mode-mixity for Voronoi lattices with different cell-regularity. All lattices have identical relative density of 0.1.

average of 20 tessellations. If, however, one considers the individual tessellations without averaging, there are considerable variations. Fig. 12 shows the results of four typical tessellations of identical cell-regularity $\Lambda = 0.5$ at a constant relative density of 0.1. Tessellations 1 exhibit an initial increase in $K_{\mathrm{eff,C}}$ followed by a drop as M increases whilst tessellation 2 shows a very similar trend to that of a regular lattice. Collectively, the data suggests that there is a 70% chance the critical effective SIF of an irregular lattice will be higher than a corresponding regular one at the same relative density for all mode-mixities $M > 0$. Also shown in Fig. 12 are the results for regular 3D tetrakaidecahedral open-cell foam by Thiyagasundaram et al. [20] where it was reported that an open-cell foam reaches a maximum $K_{\mathrm{eff,C}}$ at mode mixity $M = 0.55$ and thereafter it reduces to approximately 0.7 at $M = 1$. This is clearly different to any of the 2D Voronoi lattices studied here or reported elsewhere, such as in [5], and is the subject of a separate investigation.

The regularity of the cells in a Voronoi lattice is controlled by the global parameter Λ that merely places a constraint on the minimum cell size in the lattice. However, it has no control over the local cell topology in the vicinity of the crack tip. The differences in the results between lattices of the same Λ are indicative of the sensitivity of the lattice toughness to randomness in the local cell topology to which Λ has no control. Nonetheless, by comparing the average trend to those of individual tessellations, it allows one to make inferences, based on percentage chances, concerning the comparative toughness of the lattices for different loading modes.

4. Effects of *T*-stress

The previous section considers the lattice behaviour subjected to an asymptotic crack-tip field which neglects the non-singular terms in Eq. (7). By symmetry arguments, the second term in the series expansion of the mode I crack-tip field,

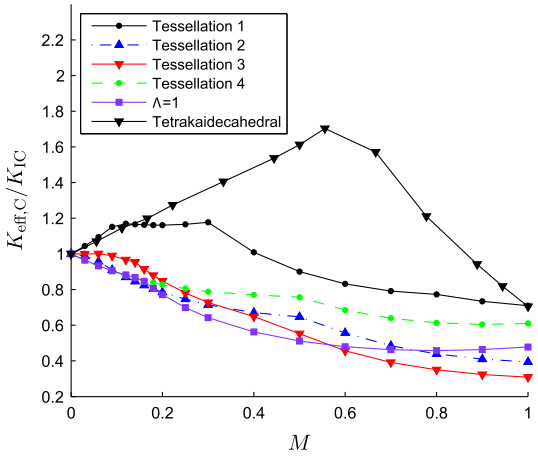

Fig. 12. Typical variations of $K_{\mathrm{eff,C}}/K_{\mathrm{IC}}$ with mode-mixity for different tessellations of the same cell-regularity $\Lambda = 0.5$. All lattices have identical relative density of 0.1.

the so-called T-stress, can be shown to vanish under mode II loading and plays a relatively minor role in fully dense elastic-brittle solids. However, Smith et al. [21] have shown that T-stress can play a role in mode II loading and only vanishes under a purely anti-symmetric loading that rarely occurs in practice. Moreover, Fleck and Qiu [5] also showed that it is necessary to include T-stress effects in order to explain the predicted fracture strength of regular hexagonal honeycomb at low relative densities. To consider the T-term, Eq. (8) must be modified to give

$$\sigma_{ij} = \frac{K_{\mathrm{I}}}{\sqrt{2\pi r}}\hat{\sigma}^{I}_{ij}(\theta) + T\delta_{1i}\delta_{1j} \quad \text{for mode I} \tag{15}$$

and

$$\sigma_{ij} = \frac{K_{\mathrm{II}}}{\sqrt{2\pi r}}\hat{\sigma}^{II}_{ij}(\theta) \quad \text{for mode II} \tag{16}$$

where δ_{ij} is the Kronecker delta. The same FE mesh in Section 3 is used here, except that the displacement components associated with the asymptotic crack-tip field in Eq. (9) is modified to include the following additional terms of

$$u_1 = \frac{\left(1 - \nu^*_{\mathrm{ps}}\right)}{2G^*_{\mathrm{ps}}} Tr\cos\theta, \quad u_2 = -\frac{\nu^*_{\mathrm{ps}}}{2G^*_{\mathrm{ps}}} Tr\sin\theta \tag{17}$$

The T-stress is typically normalised with the effective SIF in Eq. (14) to give a stress biaxiality ratio as follows [21,22]:

$$B = \frac{T\sqrt{\pi\alpha}}{K_{\mathrm{eff}}} \tag{18}$$

where α is the crack length.

Since the displacement field, Eqs. (9) and (17), was imposed on the remote boundary of the FE mesh, one tacitly assumes that the lattice is a homogeneous solid. Because no contact algorithm is incorporated into the FE model, the two sets of nodes that define the traction-free cracking plane are not allowed to come into contact, thus limiting the range of B that can be investigated. In the present study, contact between the crack planes occurs at $B > 0.3$ (for mode I) and at $B > 0$ (for mode II). For mixed-mode loading, the mode-mixity directly influences when contact between the crack planes will occur; for example, at $M = 0.5$ crack closure occurs when $B \geqslant 0.2$ as shown in Figs. 13 and 14.

Fig. 13 shows the effect of T-stress upon the normalised effective toughness, $K_{\mathrm{eff,C}}/K^0_{\mathrm{eff,C}}$, where $K^0_{\mathrm{eff,C}}$ is the corresponding critical SIF at zero T-stress. Again, the data points for $\Lambda \neq 1$ is the average of twenty realisations. It would appear that the influence of T-stress on the normalised effective toughness is most pronounced for mode I loading with negative T-stresses. The normalised effective fracture toughness of a lattice decreases rapidly with increasing negative T-stresses: at $B = -1$, the knockdown in effective toughness is, on average, nearly 75% for mode I and 50% for mode II loading. The opposite is true for positive T-stresses, since an additional negative displacement component in the x_2 direction reduces the cell deformation in the vicinity of the crack tip, leading to an enhancement of the normalised effective toughness as seen in Fig. 13. Again, mode I loading is more sensitive to the presence of positive T-stresses than mode II.

Fig. 13a shows that T-stress has the same effect upon the normalised effective toughness $K_{\mathrm{eff,C}}/K^0_{\mathrm{eff,C}}$ for both the regular and irregular lattices. At $M = 0.5$, the effective toughness of an irregular lattice is only marginally lower than a corresponding regular one for negative T-stresses. Fig. 13b compares the same for lattices of different relative densities at 0.05 and 0.1. In general, lattices of a higher relative density are less affected by a finite T-stress which agrees with Fleck and Qiu [5]. However, the knockdown in effective toughness caused by a reduction in relative density is only marginal, and comparatively insignificant, compared to the overall knockdown caused by the introduction of T-stresses. Regardless, the quadratic dependence of toughness, $K^0_{\mathrm{eff,C}}$, on relative density still holds.

Fig. 14 shows the effect of T-stress on the normalised fracture loci for lattices with $\Lambda = 0.5$ and 1. For negative T, the fracture locus expands as shown because mode I toughness is more sensitive to the inclusion of T-stresses than mixed-mode or mode II. Unlike a regular lattice with zero T-stresses, the kink is now less prominent and the switch in the initial cell wall fracture location occurs at a higher mode mixity (at $M = 0.4$ and 0.7 for $B = -0.5$ and -0.1, respectively). At $B = -1$, the $K_{\mathrm{II}}/K_{\mathrm{IC}}$ ratio becomes nearly doubled, from 0.47 to 0.95 and from 0.53 to 1.08, for a regular honeycomb and an irregular lattice ($\Lambda = 0.5$), respectively.

One likely reason for the significant contribution of T-stress to the effective macroscopic toughness of 2D lattices is their near-unity Poisson's ratio ν^*_{ps}. Referring to Eq. (17), T-stress induces additional boundary displacements which is predominantly confined to the x_2 direction, with minimal addition to the x_1 direction, if ν^*_{ps} is close to unity. Consequently, the effects of T-stress may not be as significant in a 3D lattice since their Poisson's ratio was reported to be between 0.3 and 0.5 [1], and this would somewhat suppress the effect of T-stress upon its macroscopic toughness.

5. Fracture location maps

Unlike fully dense solids, the crack path in a Voronoi lattice is, in general, discontinuous where the location of the initial cell wall fracture can, in extreme cases, occur up to six cells away from the crack-tip cell [23]. The crack-tip in the FE model is

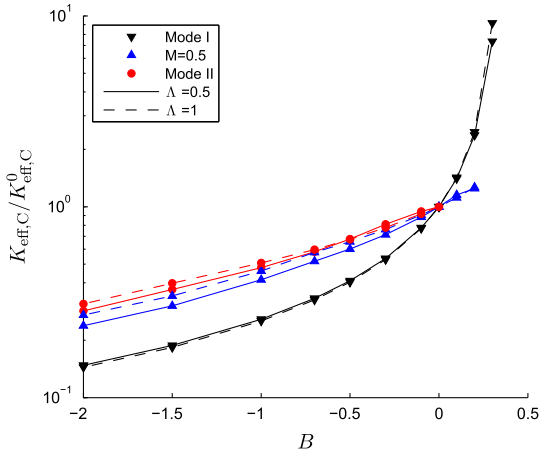

(a) Cell-irregularity effect

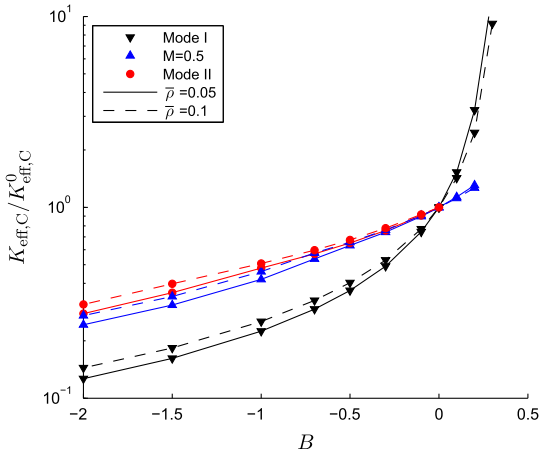

(b) Density effect

Fig. 13. Variation of the normalised toughness $K_{eff,C}/K^0_{eff,C}$ against T-stress for Voronoi lattices at two different (a) cell-regularities and (b) relative densities.

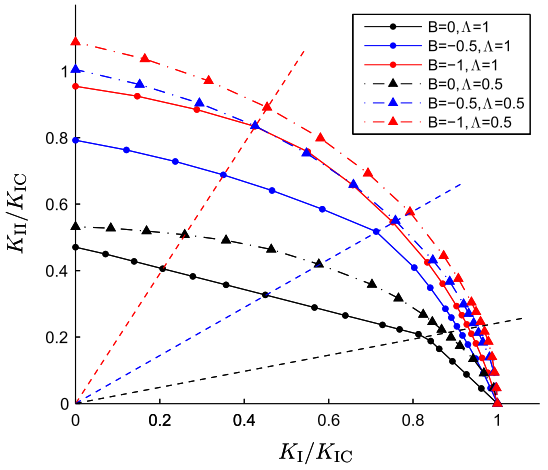

Fig. 14. Fracture loci of Voronoi lattices at increasing negative T-stress. The three straight lines correspond to $M = 0.15$, 0.4 and 0.7. All the lattices have identical relative density of 0.1. Each data point for $\Lambda = 0.5$ is the average of 20 tessellations.

assumed to coincide with the nucleus of the crack-tip cell as depicted in Fig. 15. For a perfect regular lattice, crack initiation always occurs at point A for pure mode I loading. This contrasts with the assumption made by Gibson and Ashby [1] where the cell wall immediately ahead of the crack-tip, part of the crack-tip cell, is assumed to fracture first. If mode-mixity $M \geqslant 0.15$, the fracture site switches to point B, and remains there, for all subsequent values of M, including for pure mode II. This switch coincides with a kink in the fracture locus in Fig. 9. It is worth noting that the relative density of the lattice has no effect upon the fracture location - this is consistent with that reported in [5]. For irregular lattices, local variations in the cell topology have a strong influence upon the stress magnitude in the cell walls and, consequently, the location of initial wall fracture. In addition, Fig. 10a also shows that the location of wall fracture is highly sensitive to changes in mode-mixity for the irregular lattices compared to a regular one.

Fig. 16 shows the location of the fractured cell walls for Voronoi lattices of two different relative densities (0.05 and 0.1) at three levels of mode-mixities. Each fracture location map combines the predicted fracture sites from all twenty tessellations carried out for each level of cell regularity. A dot in the failure map indicates the fracture site whilst the line indicates the orientation of the failed cell wall. The contours of constant radius give the average number of cells away from the crack-tip cell, calculated by taking the average distance of the cell vertices from the crack tip for one hundred lattices. Unsurprisingly, there is a significant amount of scatter in the observed failure sites. It is evident that the majority of the failures occurs near the crack tip, in cells adjacent to the crack-tip cell. However, fractured cell walls were also observed up to six cells away from the crack-tip cell, this is consistent with the experimental observations of Motz and Pippan [23]. As the lattice regularity decreases, the fracture location becomes increasingly dispersed which is consistent with the increased level of randomness in the cell topology. Notice that the relative density of the lattice has almost no influence over the location of fracture, this is the same for regular lattices, compare (a,b), (c,d) and (e,f) in Fig. 16.

The loading mode appears to have a strong influence over where and how the failed cell walls were clustered around the vicinity of the crack-tip. Under mode I loading, most of the fractured cell walls were clustered between the sectors of $-120^\circ \lesssim \theta \lesssim -45^\circ$ and $45^\circ \lesssim \theta \lesssim 120^\circ$ – see Fig. 16a and b. In mode II, the majority of the cracked walls were clustered between $-30^\circ \lesssim \theta \lesssim 30^\circ$ ahead of the crack-tip with significant notable exceptions behind the crack-tip. For mixed-mode loading (Fig. 16c and d shows the case for $M = 0.5$), the fractured cell walls were clustered between the sectors of $0^\circ \lesssim \theta \lesssim 45^\circ$ and $-135^\circ \lesssim \theta \lesssim -90^\circ$. As mode-mixity increases from 0 to 1, the clustering of the cracked cell walls also shifts relative to the cracking plane as depicted in Fig. 16. In general, it is observed that lattices of different cell-regularity exhibit similar clustering patterns at the same mode-mixity. Interestingly, the clustering of the fracture sites is reminiscent of the plastic zone shape predicted by standard LEFM for fully dense solids. It is important to emphasise that there is no observable correlation between the location, orientation and length of the cracked cell wall with any increase or decrease in toughness for different realisations of lattices with the same regularity Λ and relative density $\overline{\rho}$.

In the presence of finite T-stress, the clustering of the fracture sites changes dramatically. Fig. 17 shows the results for twenty lattices, with cell-regularity $\Lambda = 0.5$, subjected to mode I, mode II and mixed mode ($M = 0.5$) loadings at different stress biaxiality ratio B. An increasing T-stress alters the clustering pattern and has the effect of shifting the fractured cell walls to locations more typical of mode I loading as described above. At a high T-stress (Fig. 17 shows the case for $B = -2$), the fracture locations recorded were very similar irrespective of mode-mixity. Note also the observed locations for mode I remain unchanged at all values of B. Since the Poisson's ratio of the 2D lattices is close to unity and the inclusion of T-stress merely induces additional boundary displacement in the x_2 direction, but a comparatively negligible boundary displacement in the x_1 direction, the clustering of the fracture sites is reminiscent of that seen in the mode I loading when T-stress has a dominant effect.

The results suggest that crack propagation in a cellular material is unlikely to be a contiguous process. Depending on the mode-mixity and T-stress magnitude, the first ligament fracture occurs at seemingly random location, up to a maximum of

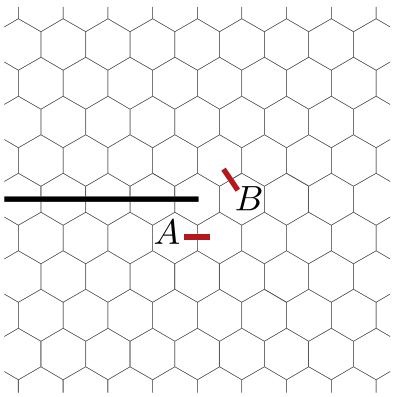

Fig. 15. Location of cell wall for a regular lattice. Points A and B indicates the location of fractured cell wall under pure mode I and mode II loadings, respectively.

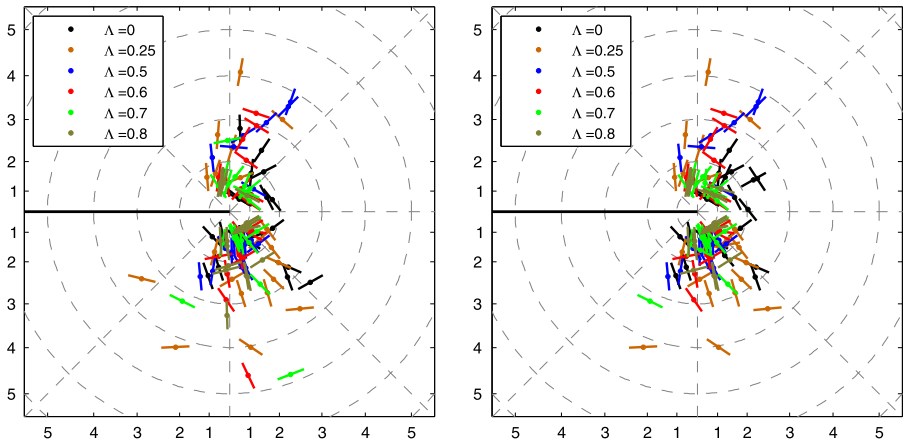

(a) $M = 0, \overline{\rho} = 0.05$ (b) $M = 0, \overline{\rho} = 0.1$

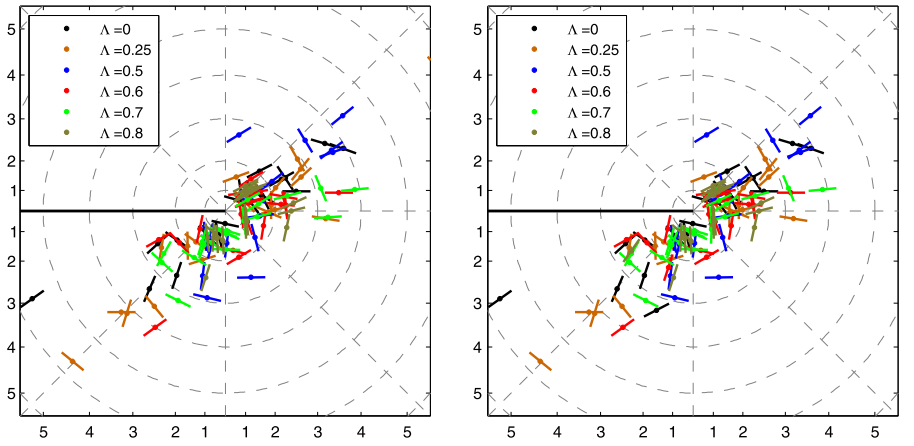

(c) $M = 0.5, \overline{\rho} = 0.05$ (d) $M = 0.5, \overline{\rho} = 0.1$

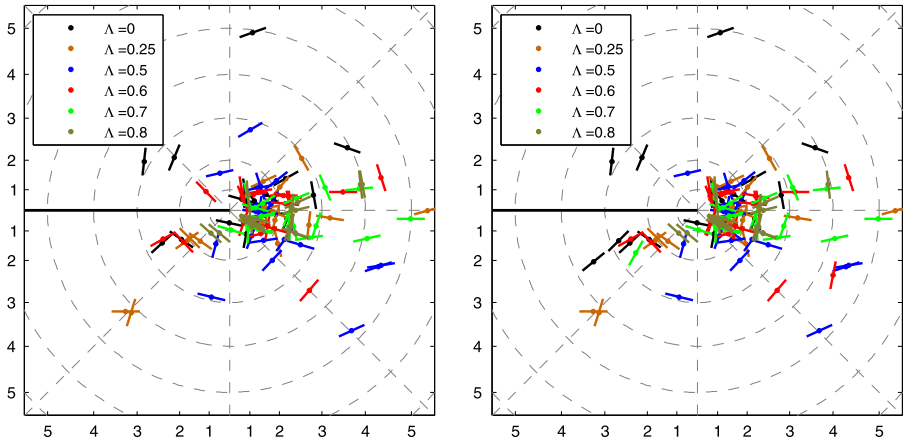

(e) $M = 1, \overline{\rho} = 0.05$ (f) $M = 1, \overline{\rho} = 0.1$

Fig. 16. The location of initial cell wall fracture in the lattices. The mid-point of the fractured cell wall is shown as a dot and the orientation of the cell wall as a line. The circular contours indicate the average distance, non-dimensionalised to give the average number of cells, away from the crack-tip cell.

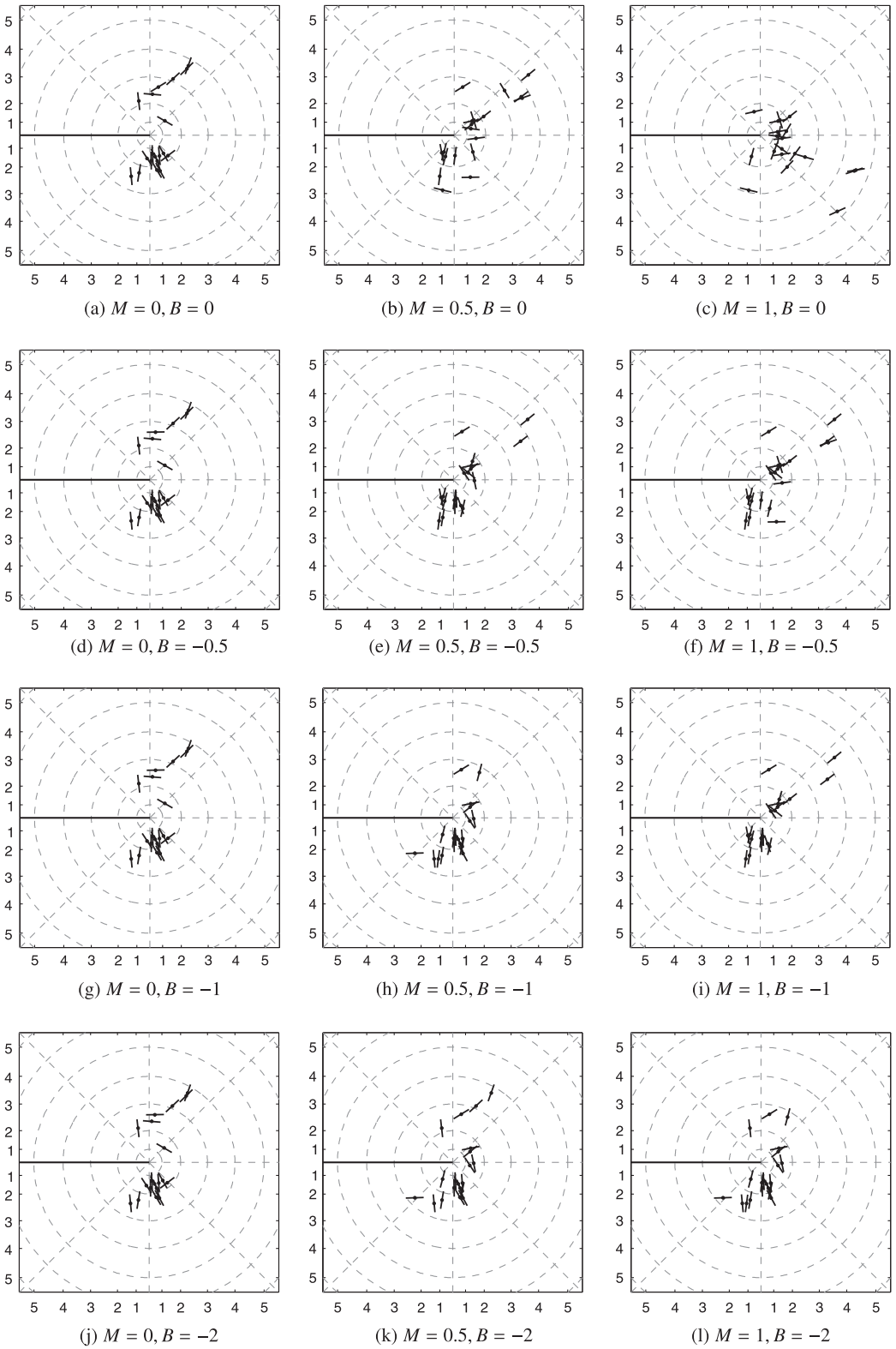

Fig. 17. Failure locations of twenty different irregular honeycombs, with $\Lambda = 0.5$. The lattices are loaded under mode I, mode II and mixed mode loading ($M = 0.5$) with various values of negative T-stress.

5–6 cells away from the crack-tip for all the cases studied here. It is, as yet unknown, how fracture of a ligament leads to the stress redistribution in other intact ligaments within the fracture process zone and how the fractured ligaments eventually link up to form a continuous crack path. This is part of an ongoing investigation which will be reported elsewhere.

6. Strain maps and energy partition

6.1. Strain maps

In this section, strain maps are generated to assist with the visualisation of the deformation field around the crack tip. The approach follows the one used by Tekoglu and Onck [13]. Each cell in the Voronoi lattice is first triangulated, using Delaunay triangulation, as shown in Fig. 18. The total number of triangles n, after triangulation, depends on how many vertices there are in a given cell.

Assuming that each triangulated region has a constant strain, or a constant strain triangle in standard FE terminology, the vertex displacements $u_i (i = 1,2)$ from the FE analysis can be used to estimate its strain. The overall or 'apparent' strain of a cell, $\varepsilon^{\text{cell}}$, is based on the weighted area-average of all the triangulated regions making up that cell. This is normalised by $\sigma_f/\overline{\rho}E_s$ to account for variations in relative density $\overline{\rho}$ and solid material properties (σ_f, E_s) as follows

$$\varepsilon^{\text{cell}} = \frac{\sum_{j=1}^{n} \varepsilon_j A_j}{\sum_{j=1}^{n} A_j}; \quad \bar{\varepsilon}^{\text{cell}} = \frac{\varepsilon^{\text{cell}}}{\sigma_f} \overline{\rho} E_s \tag{19}$$

where ε_j is the strain for triangle j, A_j is the area of triangle j and $j = 1, \ldots, n$.

Strain maps for a regular hexagonal lattice are given in Fig. 19. Even though their construction is fairly crude, the resulting strain maps reveal a smooth strain transition between cells, with regions of highly strained cells clustered around the crack tip. Examination of non-truncated lattices, of 200×200 cells (not shown here), reveal that the results are unaffected by boundary effects. Fig. 19a shows that, in mode I, the region ahead of, as well as above and below, the crack tip cell is largely in compression as opposed to the region behind the crack tip. Due to Poisson's effect, note that $v^*_{ps} \approx 1$, the opposites occurs for the strain field $\bar{\varepsilon}_{22}$ shown in Fig. 19b. In mode II, however, very high shear strain is developed in the cell next to the crack tip as shown in Fig. 19f. The location where fracture initiates in a regular hexagonal lattice for pure mode I and mode II loading corresponds to regions of either high strain gradient or high localised shear strain in the 'apparent' strain maps.

Fig. 20 gives the strain maps for an irregular Voronoi lattice. Notice that the strain fields are substantively different to the regular ones. They are no longer smooth and bands of highly strained cells are scattered throughout the lattice. Unusually high level of strains are normally observed only in isolated cells, such as in Fig. 20a. By contrast, moderate strain levels seem to occur in bands of cells as seen in Fig. 20b. For the majority of the cases, fracture initiation does coincide with a region of elevated 'apparent' strain which is consistent with that observed for a regular lattice. However, this is not always the case as seen in Fig. 20c. It would seem that the cell deformation is extremely sensitive to microstructural variations at the cell scale which is the reason for the variability in the results.

6.2. Strain energy partition

The elastic strain energy of a lattice can be partitioned into the various contributions from bending (U_b), axial stretch (U_a) and shear (U_s) according to

$$U_b = \frac{M^2 l}{2E_s I}, \quad U_a = \frac{F_1^2 l}{2E_s A}, \quad U_s = \frac{\psi F_2^2 l}{2G_s A} \tag{20}$$

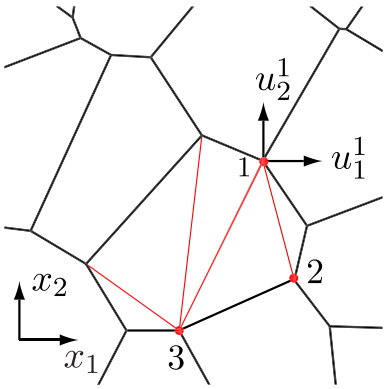

Fig. 18. Delaunay triangulation of a single cell with seven vertices which gives five triangles, shown in red, following triangulation. (For interpretation of the references to color in this figure legend, the reader is referred to the web version of this article.)

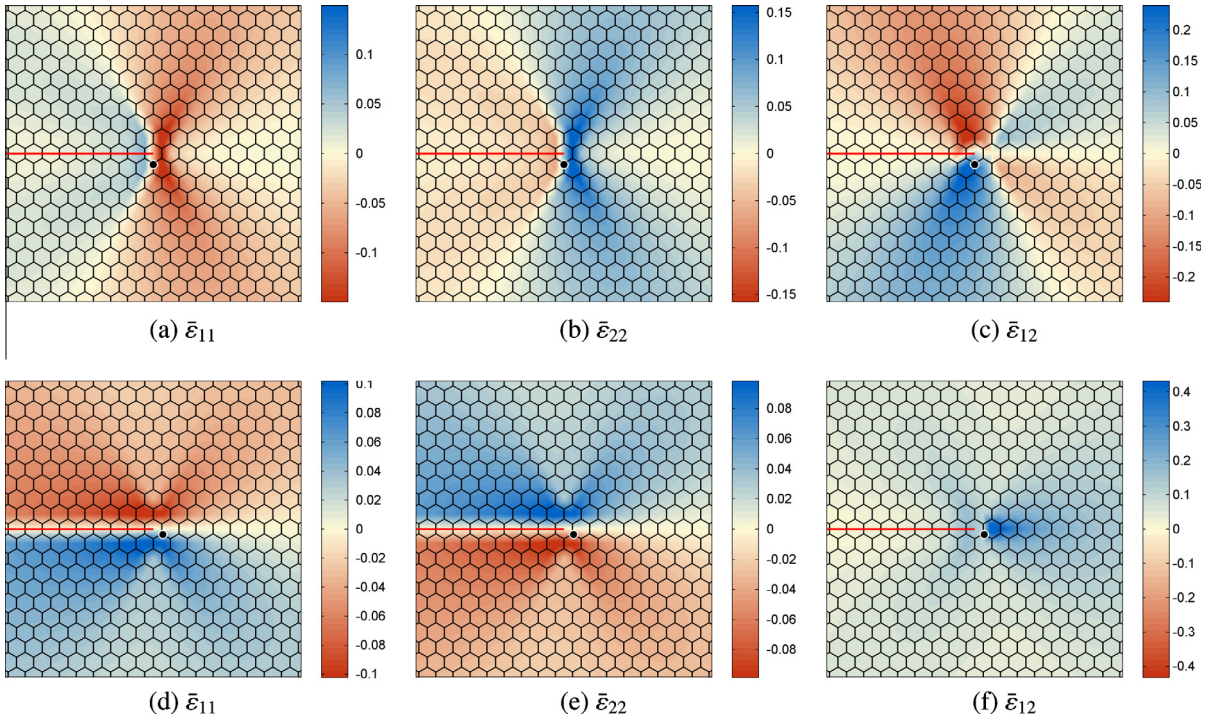

Fig. 19. Strain maps for regular hexagonal honeycomb. (a)–(c) are for mode I loading and (d)–(f) for mode II. The dot (•) indicates the location of the fractured cell wall.

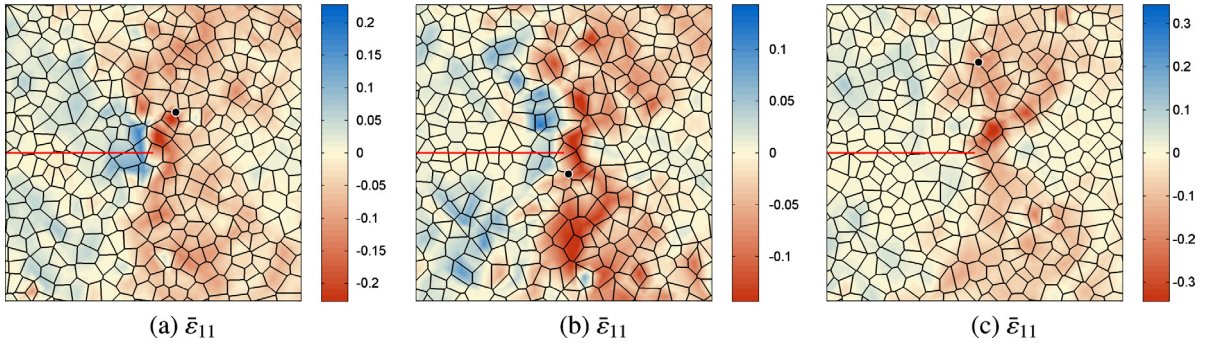

Fig. 20. Strain maps for three different tessellations of a Voronoi lattice, with cell-regularity $\Lambda = 0.5$, subjected to mode I loading. The dot (•) indicates the location of the fractured cell.

where M is the bending moment, F_1 the axial force, F_2 the shear force, l is the length of a beam element, I the second moment of area and ψ is a constant depending on the cross-sectional geometry of the cell wall. It is estimated that $\psi = 1.15$ for a rectangular cross-section. From Eq. (20), the ratio of the bending strain energy to the total strain energy is estimated as follows:

$$\eta = \frac{U_b}{U_b + U_a + U_s}. \tag{21}$$

When fracture initiates in any of the cell wall, the bending strain energy ratio η and the normalised maximum stress σ_{max}/σ_f are calculated for each element in the FE mesh. Note that there can only be one element in each mesh whereby $\sigma_{max}/\sigma_f = 1$. The elements are then reordered in increasing η value; this is given by the blue lines shown in Figs. 21–23. Their corresponding normalised maximum stress is shown in red and the horizontal axis gives the percentage number of elements with η less than the corresponding value indicated in the vertical axis. Using these plots, the dominant deformation mode in the fractured cell wall can be identified. In the subsequent discussions, the dominant mode of deformation in an element is bending if $\eta \geqslant 0.8$.

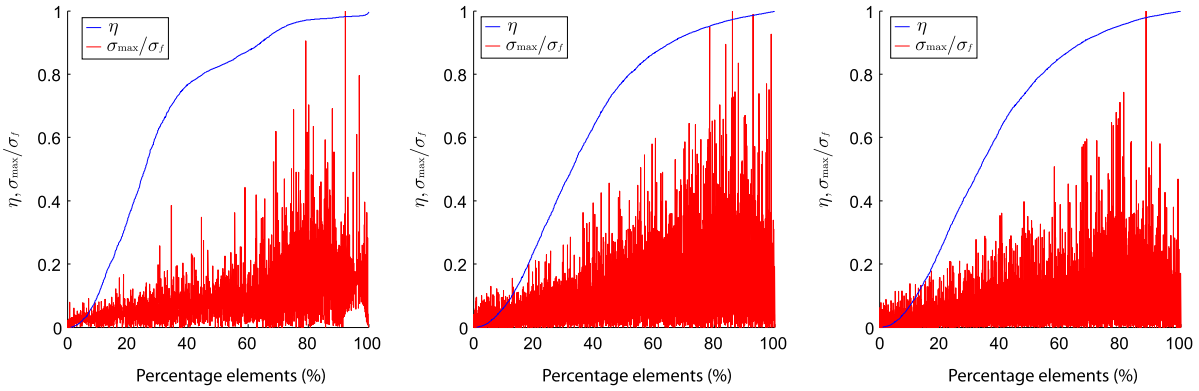

Fig. 21. Effects of cell regularity on lattices with relative density $\overline{\rho} = 0.1$ subjected to mode I loading.

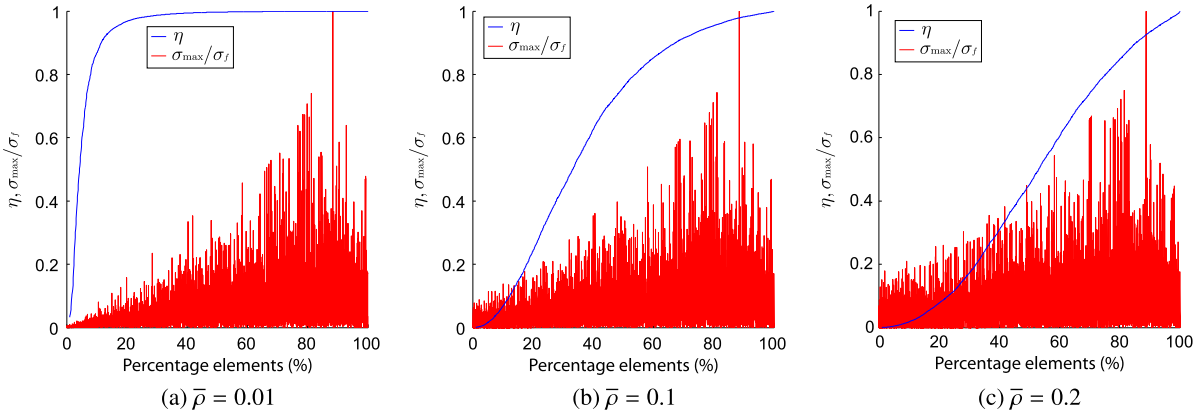

Fig. 22. Effects of relative density on an irregular ($\Lambda \to 0^+$) lattice subjected to mode I loading.

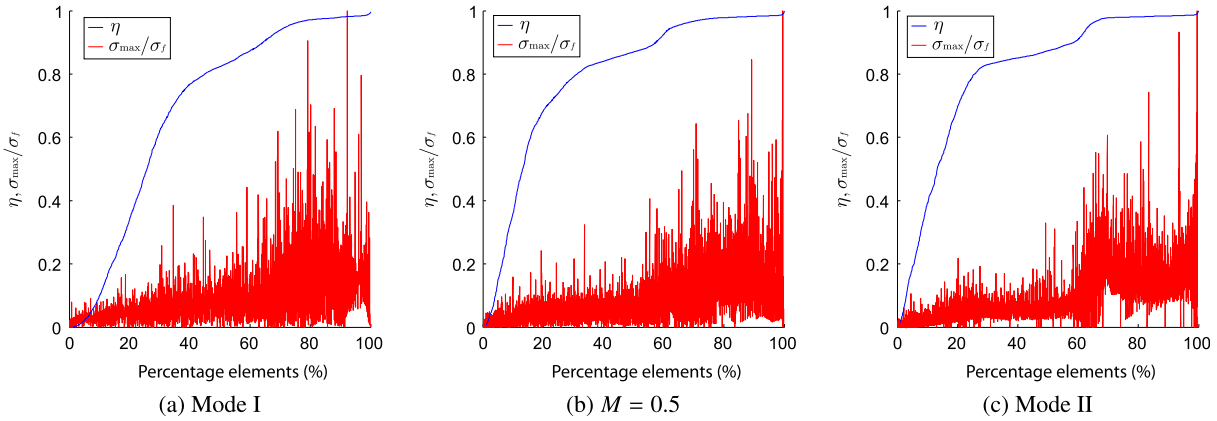

Fig. 23. Effects of mode mixity on a regular lattice with relative density $\overline{\rho} = 0.1$.

Fig. 21 shows the effect of cell regularity upon η and σ_{max}/σ_f for a lattice with relative density $\overline{\rho} = 0.1$, subjected to mode I loading. For a regular lattice, fracture initiates in cell wall whereby bending is the dominant mode of deformation; this is clearly evident in Fig. 21a. The effects of increasing the relative density of a lattice is shown in Fig. 22. At low relative density, say $\overline{\rho} = 0.01$, most elements deform primarily in bending; Fig. 22a shows that nearly 90% of the elements in the FE mesh have $\eta > 0.8$. Unsurprisingly, the number of elements where bending is the dominant mode of deformation decreases with

increasing relative density $\overline{\rho}$ as the cell walls become stockier. At $\overline{\rho} = 0.2$, less than 25% of the elements deform primarily in bending with axial stretch and shear becoming increasingly dominant in the rest of the elements. It would appear that cell wall fracture is predominantly a result of bending deformation, regardless of relative density, as shown in Fig. 22. Note that the present study only considers $\overline{\rho} \leqslant 0.3$. Fig. 23 shows the effect of mode-mixity upon η and σ_{max}/σ_f for a regular lattice. As mode mixity increases from zero (pure mode I) to one (pure mode II), increasing number of elements experience a switch in their deformation mode towards bending. However, the results show that mode-mixity, again, does not the alter the dominant mode of deformation experience by the cell wall prior to fracture, i.e. it remains predominantly by bending. Figs. 21–23 reveal that fracture initiation in a Voronoi lattice is always a bending-dominated process and only occurs in cell walls that experience high level of bending deformation regardless of relative density, mode-mixity or cell regularity. This is the reason why the fracture toughness of a Voronoi lattice always scales with $\overline{\rho}^2$.

7. Concluding remarks

The fracture toughness and location of fracture initiation were studied for Voronoi lattices with varying degree of cell-regularity. The pure mode I toughness of a lattice decreases as it becomes more irregular with an overall reduction of up to 25% for completely random lattices. There is no indication that pure mode II fracture toughness is affected significantly by cell irregularities. The macroscopic toughness of the lattices was found to have a quadratic dependence upon relative density for all values of Λ because of their bending dominated response. By partitioning of the strain energy, it is shown that axial stretch contributes to less than 10% of the overall deformation of the cracked cell wall regardless of the relative density, cell regularity and mode-mixity. The Voronoi lattices, whether regular or irregular, have a greater resistance to mode I than mode II loading. The mode I toughness of the lattices are more sensitive to cell topological variations in the vicinity of the crack tip than mode II. Fracture loci for the lattices are obtained in combined mode I and mode II stress intensity factor space. Although there are considerable variations between the fracture locus of different tessellations with the same Λ, this study shows there is a 70% chance the critical effective SIF of an irregular lattice will be greater than a corresponding regular one of the same relative density for all mode mixities $M > 0$. The effects of including T-stress was also investigated where a significant decrease/increase in fracture toughness is observed: for example, at $B = -1$, the knockdown in the effective toughness of the lattice is nearly 75% for mode I and 50% for mode II loadings. This trend reverses with positive T-stresses. The present study found that the knockdown/enhancement in toughness caused by changes in relative density or cell-regularity is insignificant when compared to the overall knockdown/enhancement due to the inclusion of a T-stress.

Fracture location maps are obtained for lattices with different cell-regularities, mode-mixities, relative densities and T-stresses. Significant scatter in the initial cell wall fracture location is observed: the majority of failed cell walls occur near the crack tip, although they are also observed at up to five cells away from the crack-tip cell, suggesting a highly discontinuous cracking path that is bridged by many un-cracked ligaments. As mode-mixity changes from mode I to mode II, the clustering of the fractured cell walls shifts relative to the crack plane and is reminiscent of the evolution of the plastic zone shape in fully dense solids from LEFM. The introduction of a T-stress changes considerably the clustering of the fractured cell walls: mode I remains, in general, unaffected, whilst for mode II and mixed mode loadings at high T-stresses, the clustering is reminiscent of that seen in mode I loading. There is no correlation between the calculated fracture toughness for different lattice realisations, with the same Λ and $\overline{\rho}$, and the location where cell wall cracking first initiates. 'Apparent' strain maps show that the location of cracking is dictated by the local deformation, typically in a region with either highly localised strain or high strain gradients.

Acknowledgement

The first author is grateful to the EPSRC (UK) for financial support provided through a 2010/11 doctoral training grant awarded to University College London.

References

[1] Gibson LJ, Ashby MF. Cellular solids: structure and properties. UK: Cambridge University Press; 1997.
[2] Currey JD. The mechanical adaptations of bones. Princeton, NJ: Princeton University Press; 1984.
[3] Ladd AC, Kinney JH, Haupt DL, Goldstein SA. Finite-element modeling of trabecular bone: comparison with mechanical testing and determination of tissue modulus. J Orthopaed Res 1998;16:622–8.
[4] Heaney R. Is the paradigm shifting? Bone 2003;33(4):457–65.
[5] Fleck NA, Qiu X. The damage tolerance of elastic-brittle, two-dimensional isotropic lattices. J Mech Phys Solids 2007;55:562–88.
[6] Romijn NER, Fleck NA. The fracture toughness of planar lattices: imperfection sensitivity. J Mech Phys Solids 2007;55:2538–64.
[7] Choi S, Sankar BV. A micromechanical method to predict the fracture toughness of cellular materials. Int J Solids Struct 2005;42:1797–817.
[8] Maiti SK, Ashby MF, Gibson LJ. Fracture toughness of brittle cellular solids. Scripta Metall Mater 1984;18:213–7.
[9] Huang JS, Gibson LJ. Fracture toughness of brittle honeycombs. Acta Metall Mater 1991;39:1617–26.
[10] Silva MJ, Hayes WC, Gibson LJ. The effects of non-periodic microstructure on the elastic properties of two-dimensional cellular solids. Int J Mech Sci 1995;37:1161–77.
[11] Silva MJ, Gibson LJ. The effects of non-periodic microstructure and defects on the compressive strength of two-dimensional cellular solids. Int J Mech Sci 1997;39:549–63.
[12] Gibson LJ. Biomechanics of cellular solids. J Biomech 2005;38:377–99.

[13] Tekoglu C, Onck PR. Size effects in two-dimensional voronoi foams: a comparison between generalized continua and discrete models. J Mech Phys Solids 2008;56:3541–64.
[14] de Berg M, van Kreveld M, Overmars M, Schwarzkopf O. Computational geometry: algorithms and applications. 2 ed. Berlin Heidelberg: Springer-Verlag; 2000.
[15] Zhu HX, Hobdell JR, Windle AH. Effects of cell irregularity on the elastic properties of 2D Voronoi honeycombs. J Mech Phys Solids 2001;49:857–70.
[16] Chen C, Lu TJ, Fleck NA. Effect of imperfections on the yielding of two-dimensional foams. J Mech Phys Solids 1999;47:2235–72.
[17] Williams ML. On the stress distribution at the base of a stationary crack. J Appl Mech 1957;24:109–14.
[18] Kanninen MF, Popelar CH. Advanced fracture mechanics. New York: OUP; 1985.
[19] Shih CF. Small-scale yielding analysis of mixed mode plane-strain crack problems. ASTM STP 1974;560:187–210.
[20] Thiyagasundaram P, Wang J, Sankar BV, Arakere NK. Fracture toughness of foams with tetrakaidecahedral unit cells using finite element based micromechanics. Engng Fract Mech 2011;78(6):1277–88.
[21] Smith DJ, Ayatollahi MR, Pavier MJ. On the consequences of *T*-stress in elastic brittle fracture. Proc R Soc A 2006;462:2415–37.
[22] Leevers PS, Radon JC. Inherent stress biaxiality in various fracture specimen geometries. Int J Fracture 1982;19:311–25.
[23] Motz S, Pippan R. Fracture behaviour and fracture toughness of ductile closed-cell metallic foams. Acta Mater 2002;50:2013–33.